Supplemental Information For

Li-ion and Na-ion intercalation in layered MnO$_2$ cathodes enabled by using bismuth as a cation pillar

Matthew A. Kim [1], Eric K. Zimmerer [1], Zachary T. Piontkowski [2], Mark A. Rodriguez [3], Noah B. Schorr [4], Bryan R. Wygant [4], John S. Okasinski [5], Andrew C. Chuang [5], Timothy N. Lambert [4], and Joshua W. Gallaway [*, 1]

1. Department of Chemical Engineering, Northeastern University, 360 Huntington Avenue, Boston, MA 02115, USA.

2. Department of Applied Optical and Plasma Science, Sandia National Laboratories, Albuquerque, New Mexico 87185, USA

3. Materials Characterization and Performance Department, Sandia National Laboratories, Albuquerque, New Mexico 87185, USA

4. Department of Photovoltaics and Materials Technology, Sandia National Laboratories; Albuquerque, New Mexico, USA, 87185, USA.

5. X-ray Science Division, Advanced Photon Source, Argonne National Laboratory, Lemont, Illinois 60439, USA.

* Corresponding author, j.gallaway@northeastern.edu

1. Supplemental Methods

Synthesis of layered MnO$_2$ materials. While we found a linear relationship between the initial and final Bi:Mn ratios (see **Fig S1**), the Bi:Mn ratio was always enriched in the synthesized material, as can be seen in **Table 1**. This was because soluble Mn products were removed during the washing step following the solid-state synthesis. These were K$_2$MnO$_4$ and K$_3$MnO$_4$, which were soluble in water. Although we did not analyze the filtrate, this is presumably because fewer soluble Bi-containing species were removed by the washing.

K-extraction of materials. Chemical extraction of K$^+$ from Bi^{3+} doped layered MnO$_2$ was explored. Two distinct methods are reported in the literature. A modified method proposed by Yang *et al.* was used to extract K$^+$.[1] Layered MnO$_2$ was added to a 0.5 M solution of (NH$_4$)$_2$S$_2$O$_4$ at a controlled pH of 0.2 using H$_2$SO$_4$ followed by continuous stirring at 300 rpm at 60 °C for 7 hours before being washed with DI water and dried under vacuum overnight at room temperature. Hatakeyama *et al.* proposed a K$^+$ extraction method calling for the soaking of δ-MnO$_2$ in a 0.4 M HCl solution for 50 minutes followed by washing.[2] Both methods of K$^+$ extraction were used for Bi^{3+} doped δ-MnO$_2$ (Hi-Bi).

Synthesis of Na-inserted material. It was also desired to synthesize a material that would be useful as a cathode material for Na$^+$ batteries but that was also doped with Bi^{3+} for added stability. NaMnO$_4$ has also been reported to form a crystalline layered MnO$_2$ with Na$^+$ in its interlayer.[3] The procedure for calcination of KMnO$_4$ mixed with Bi(NO$_3$)$_3$ was repeated with NaMnO$_4$ replacing KMnO$_4$. Na(NO$_3$)$_3$ was mixed with Bi(NO$_3$)$_3$ in a Mn:Bi stoichiometric ratio of 1:0.025 and calcined at 900 °C for 900 minutes. In the resulting materials, Raman bands at 570 cm^{-1} and 635 cm^{-1} were both present as would be expected for a layered MnO$_2$, as well as the band at around 410 cm^{-1} also being associated with more crystalline δ-MnO$_2$. For this reason, it was concluded that δ-MnO$_2$ with Na$^+$ as well as Bi^{3+} in the interlayer was successfully created.

However, it decomposed exceedingly quickly when exposed to air. For this reason, all battery work was performed with K-inserted materials.

Solids processing. The active material was processed by high energy ball milling (SPEX 8000M Mixer Mill) for 18 minutes in argon gas or dry air followed by sieving through a 26 μm mesh. Only the small particles that passed through the sieve were used for cathode production. The 18-minute milling time was experimentally determined to be the optimal time of milling, based on battery performance. While Lo-Bi could likely be processed using a broader range of milling time, Hi-Bi was particularly sensitive to milling time and the best performance was found at 18 minutes. This was chosen as the standardized time for both materials.

2. Supplemental Table

Table S1. Materials in pristine, uncycled cells via EDXRD analyses in **Figs 7** and **9**.

System	Cathode active material	Smaller d material	Larger d material
Li-ion	Hi-Bi	LMO spinel	dehydrated K-MnO$_2$
	Lo-Bi	LMO spinel	hydrated birnessite
Na-ion	Hi-Bi	dehydrated Na-MnO$_2$	dehydrated K-MnO$_2$
	Lo-Bi	dehydrated Na-MnO$_2$ (trace)	hydrated birnessite

EDXRD analysis revealed the pristine, uncycled cathode active material was different than the dry, as-synthesized material. This was observed in the EDXRD plots in **Figs 7** and **9**. An accounting of the uncycled materials observed in the cells is given in **Table S1**. This showed the interlayer environments within the cells were different. Layered MnO$_2$ is known to be an ion exchange material, so this result was not unexpected.

Thus in the Na-ion electrolyte both Lo-Bi and Hi-Bi produced a sodiated layered MnO$_2$ phase. The overall specific capacity was a function of the relative amounts of each of these materials, as well as the extent to which each material was electrochemically active. All of these materials showed electrochemical activity, as their Bragg reflections cycled in a manner correlated with the cell cycling. Thus, while the No-Bi material showed lower initial specific capacity than Lo-Bi and Hi-Bi in the Na-ion system (see **Fig 8**), this was a consequence of the ion exchange that took place upon wetting.

A universal finding was that the No-Bi material that had no incorporated Bi resulted in non-crystalline active material within the wetted cells (see **Fig S16**). Presumably this was due to amorphization during ion exchange. Thus Bi doping maintained crystallinity at both Lo-Bi and Hi-Bi levels in both Li-ion and Na-ion electrolytes.
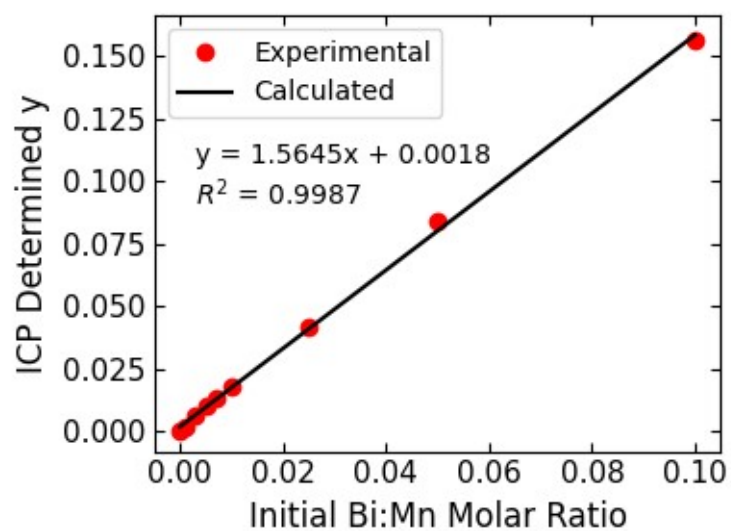
3. Supplemental Figures

Figure S1. ICP-AES determined molar fractions of Bi^{3+} dopant vs. the initial Bi:Mn molar ratio shows that at concentrations of y ≤ 0.156 the concentration of dopant could be well controlled.
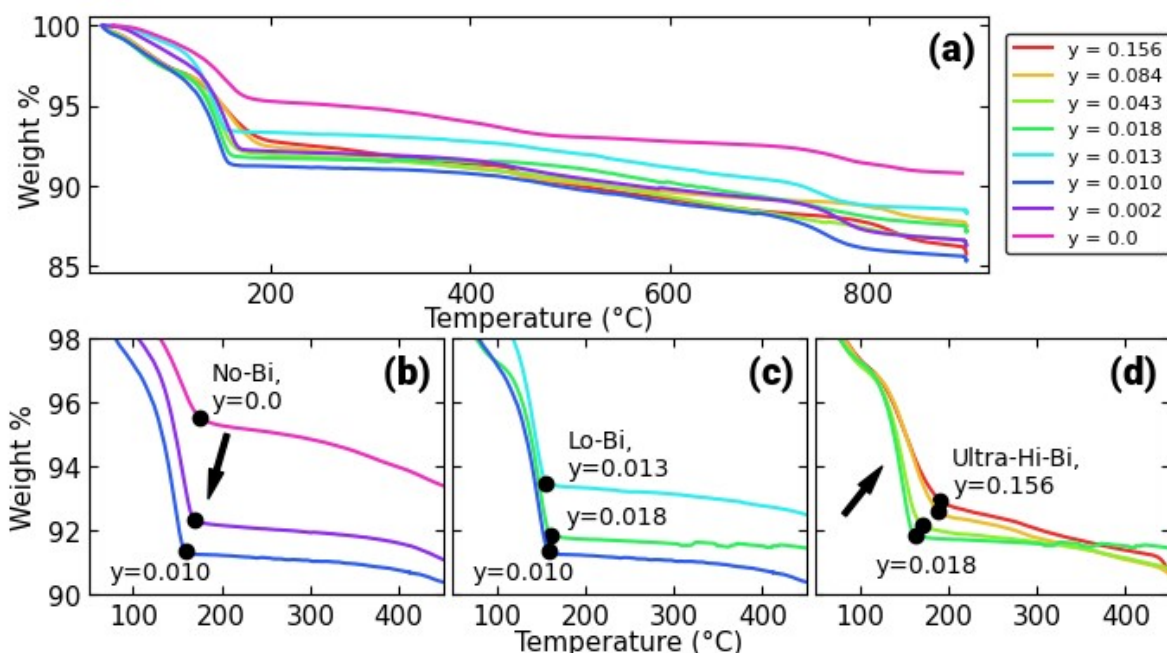
Figure S2. (a) TGA measurements were taken of all K_xBi_y-MnO_2 • nH_2O samples. (b) Comparison of samples below y = 0.013 showed that increased Bi^{3+} dopant correlated positively with amount of interlayer H_2O. (c) Comparison of concentrations from y = 0.013-0.018 showed that trends broke down in this range. (d) Comparison of samples above y = 0.018 showed that as y increased there was less interlayer water. Any change in mass below 120 °C was attributed to surface adsorbed H_2O.[141] The temperature at which the release of interlayer H_2O ceased were manually determined. These points are shown as black dots.

At lower values of y there was a direct relationship between the amount of interlayer water and the amount of Bi^{3+} dopant. Shown in **Fig S2b**, as y increased there was a greater amount of weight loss, presumably due to the release of interlayer H_2O, and the temperature at which this H_2O is released decreased. At values of y = 0.010 and below, Bi^{3+} dopant increased the amount of interlayer water present in layered MnO_2 in ambient conditions. This was consistent with prior reports. Johnson *et al*. dehydrated birnessites, differing only in inserted cations, at increasing temperatures and found that a cation's hydration energy in solution had an inverse correlation with how strongly that cation could hold onto water when in birnessite's interlayer.[137] As valence increases and as ionic radius decreases hydration energy decreases making dehydration more difficult. The much larger ionic radius of K^+ (1.52 Å) relative to Li^+ (0.9 Å) leads to it having a greater hydration energy (ΔH = -321 and -515 kJ/mol respectively), therefore holding onto water more weakly.[138] The similarities in ionic radii of Ca^{2+} (1.14 Å) and Na^+ (1.16 Å) show the significant effect valence has on the hydration energy (ΔH = -1521 and -405 kJ/mol, respectively) as Ca^{2+} has a hydration energy more than three times lower than that of Na^+ indicating that it holds onto water much more strongly. The ionic radius of Bi^{3+} (1.17 Å) is very similar to that of Na^+ (1.16 Å) indicating that it would have a much higher charge density and a significantly lower hydration energy and therefore hold onto water when in birnessite's interlayer space more tightly than K^+ or Na^+.[139,140] For example, the hydration energy of other trivalent cations in solution such as Pu^{3+} and La^{3+} are ΔH = -3441 and -3283 kJ/mol, respectively.[138] Therefore, it makes sense that the increased amount of Bi^{3+} would be correlated with increased amounts of interlayer water.

However, above the critical concentration of y = 0.013 there was a negative correlation in the amount of interlayer water and the Bi^{3+} dopant. As y increased the amount of water released before the beginning of the heating plateau decreased, shown in **Fig S2d**. This was likely due to interlayer site occupation by Bi^{3+} and K^+ displacing any H_2O that would otherwise be present.
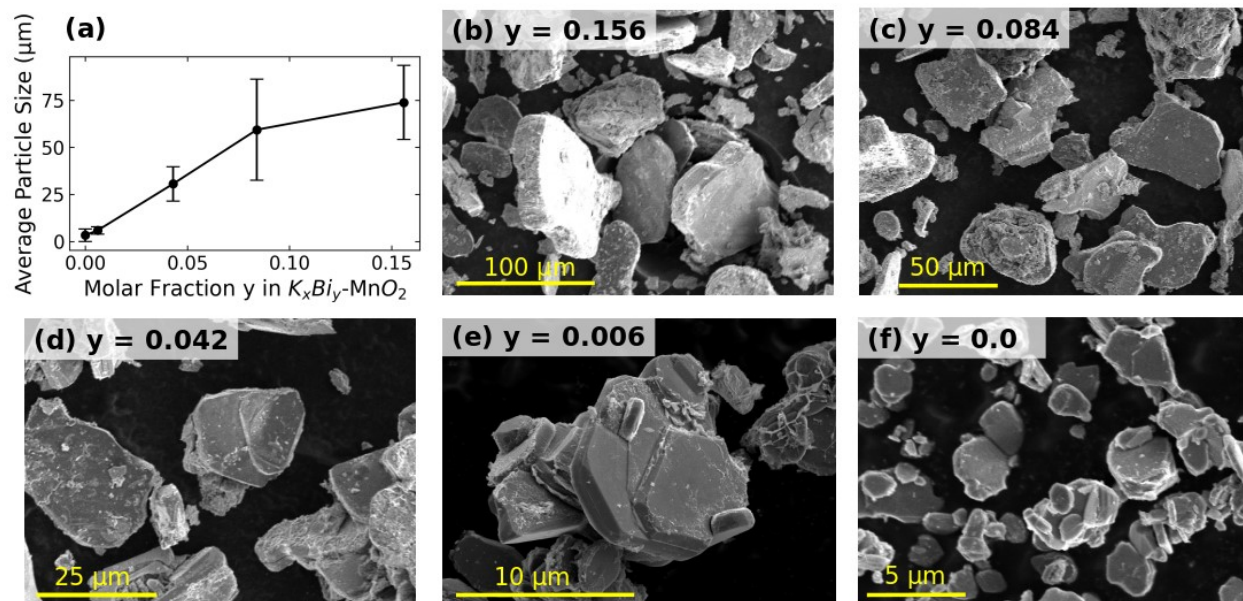
Figure S3. (a) The average particle size of K_xBi_y-$MnO_2 \cdot nH_2O$ as a function of Bi amount y. (b) y = 0.156, (c) y = 0.084, (d) y = 0.043, (e) y = 0.006, and (f) y = 0.0. These particle sizes were measured manually and averaged. Only well-formed particles with proper orientation to the SEM detector were considered in the measurements.

Fig S3a showed a logarithmic plateau of particle size with increasing y. This indicated an upper ceiling in the total amount of Bi^{3+} that can be inserted, with any additional $Bi(NO_3)_3$ precursor leading to impurities. Initial Bi:Mn ratios above 0.1 were attempted, such as 0.33 and 1. However, SEM images and XRD patterns of these materials showed impurities ($Bi_6O_6(NO_3)_4(OH)_2$ and $Bi_6O_5(NO_3)_5(OH)_3$) with no increase in average particle size relative to the y = 0.156 concentration.
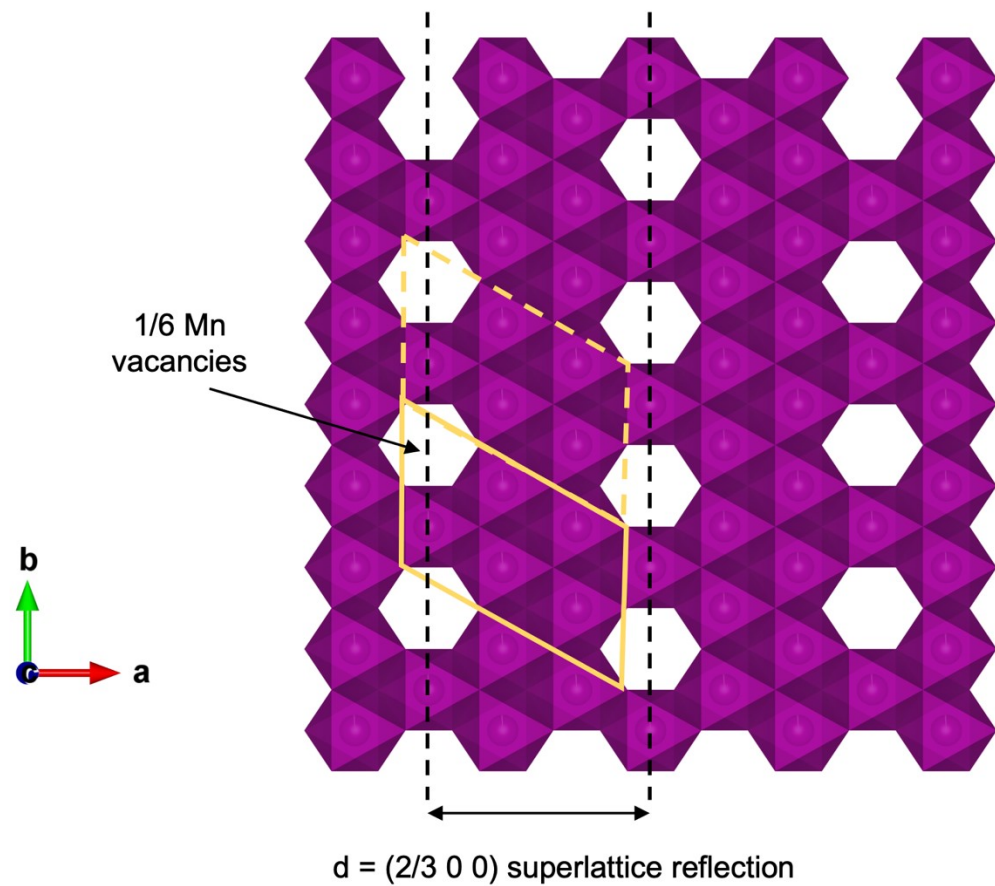
1/6 Mn vacancies

b

c ⟶ a

d = (2/3 0 0) superlattice reflection

Figure S4. Illustration of 1/6 Mn vacancies as shown in the work of Kuma et al. 1994. When the interlayer is populated by multivalent ions, a superlattice reflection is expected at about 7.8 A. This is caused by structural ordering of interlayer species in relation to the Mn vacancies. Bi^{3+} cations in particular were likely situated by Mn vacancies due to the large positive charge density that must be balanced.
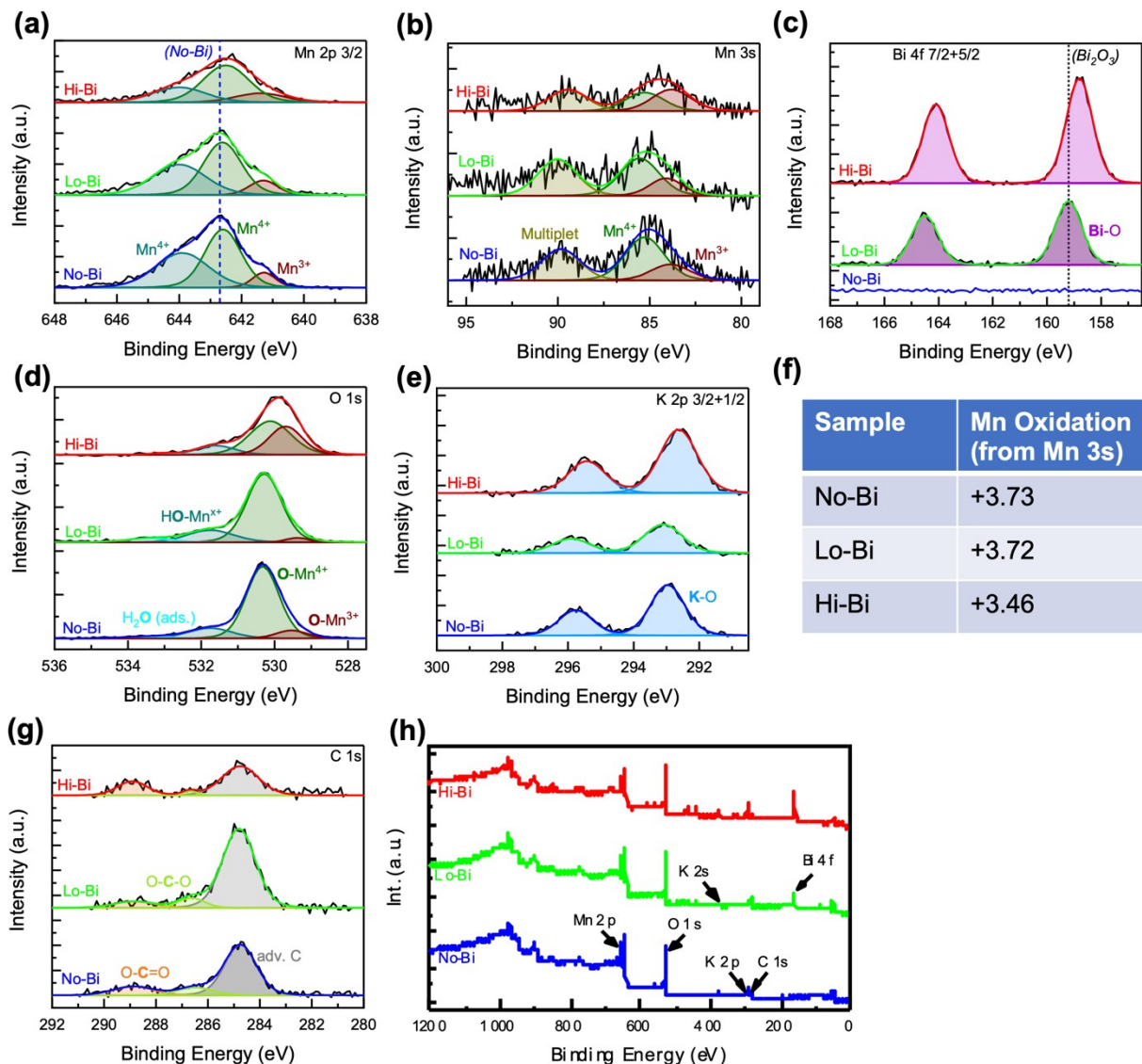
Figure S5. XPS analysis of No-Bi, Lo-Bi, and Hi-Bi materials. (a) Mn 2p 3/2 spectra with associated fits. (b) Mn 3s spectra and associated fits. (c) Bi 4f 7/2 and 5/2 spectra. (d) O 1s spectra and associated fits for various M-O species. (e) K 2p 3/2 and ½ spectra. (f) Mn oxidation state calculated from Mn 3s. (g) C 1s spectra with associated fits for adv. sp^3 carbon and oxidized C species. (h) Survey spectra of birnessite samples with primary peaks highlighted.

As Bi increased, the average Mn oxidation state shifted to lower BE (more reduced), as reflected in increased 4+/3+ area ratio and shift in main Mn 2p 3/2 peak (blue dashed line in **Fig S5a**). In **Fig S5b**, Mn 3s also showed a marked increase in Mn(III) for Hi-Bi, and a decrease of roughly 0.25 in calculated Mn oxidation state. Increased Bi likewise resulted in more reduced Bi species. Lo-Bi showed a Bi_2O_3-like species, while Hi-Bi was more reduced. Hi-Bi had a more Mn(III)-O rich spectrum than No- and Lo-Bi samples. The K in Hi-Bi was more reduced than in the No- and Lo-Bi samples. Clean fit with a single species indicated a single K-O bond with a variable binding environment. The primary adventitious/sp^3 carbon peak was used to correct other BE. Ether and carboxylic acid moieties from surface C layer also were present in all samples. Survey spectra are clean and show only the expected species present in all samples.

Atomic ratios were calculated and are shown in **Table S2**. These are shown compared to the ICP-AES results. Bi/Mn ratio varied significantly between the two techniques, with XPS appearing to show a more

Bi-rich surface than the bulk measurement from ICP-AES. This suggested a Bi-rich surface region. K/Mn ratios from both techniques were much closer and provided confidence in variation observed in the Bi/Mn quantification.

Table S2. XPS results.

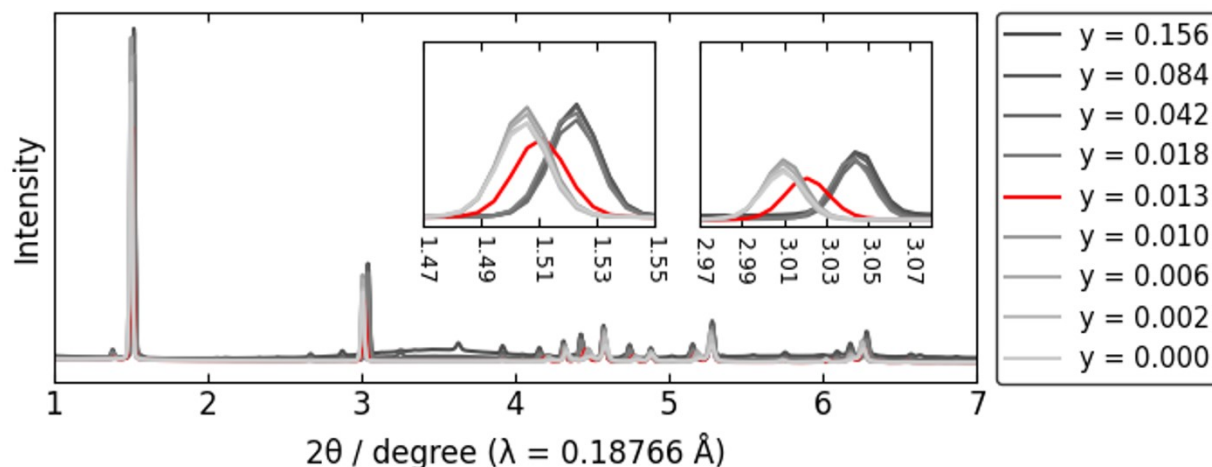| Technique	Bi/Mn Ratio		K/Mn Ratio	
	ICP-AES	XPS	ICP-AES	XPS
No-Bi	N/A	N/A	0.308	0.318
Lo-Bi	0.013	0.135	0.332	0.313
Hi-Bi	0.043	0.320	0.384	0.347

Figure S6. XPD measurements were taken of K_xBi_y-MnO_2 at 9 concentrations of Bi dopant represented as molar fraction y. All patterns are super imposed using a gray scale except for the critical concentration y = 0.013 (in red) to highlight the sudden transition of the characteristic peaks of layered MnO_2, shown in the insets.

There were some impurity peaks that emerged as y increased. The broad peak centered at 2θ = 3.5° (red data) was due to amorphous $Bi_6O_6(NO_3)_4(OH)_2$ and $Bi_6O_5(NO_3)_5(OH)_3$ impurities, which emerged only at high Bi:Mn molar ratios of y ≥ 0.156.[4, 5] Other impurities were α-Bi_2O_3 and β-Bi_2O_3, having their most intense peaks at 3.2° (27.4° CuKα) and 3.3° (28.0° CuKα).[6, 7] Given the relative intensities of these peaks in both bismuth oxides they were unlikely to be represented at other positions in the diffraction patterns, particularly at y ≤ 0.042.
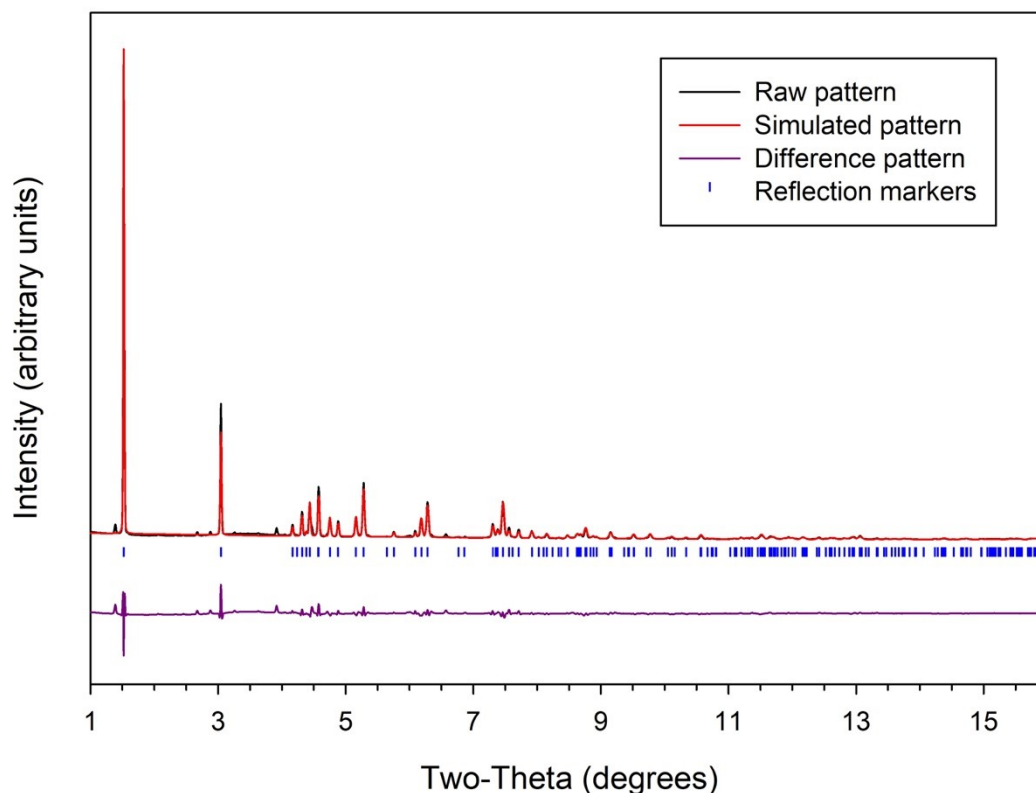
Figure S7. Rietveld refinement of the Hi-Bi material. Observed, simulated, and difference patterns for the fit are provided, as well as the markers locations for the refined hkl locations. The final residual error for the refinement was RB = 10.82%.

Table S3 reports refined lattice parameter values for the No-Bi, Lo-Bi, and Hi-Bi compositions as compared to the structure reported by Gaillot, et al., (2007). Cell parameters were obtained via Rietveld refinement of X-ray diffraction patterns and performed via JadePro version 8.7 (Materials Data, Inc.) XRD analysis software. Comparing the reference material to the No-Bi case, the larger unit cell in PDF entry 04-014-5768 is likely due to the higher water and higher K presence in that structure.

Table S3. Refined lattice parameters. Space group 63, orthorhombic, Cmcm.

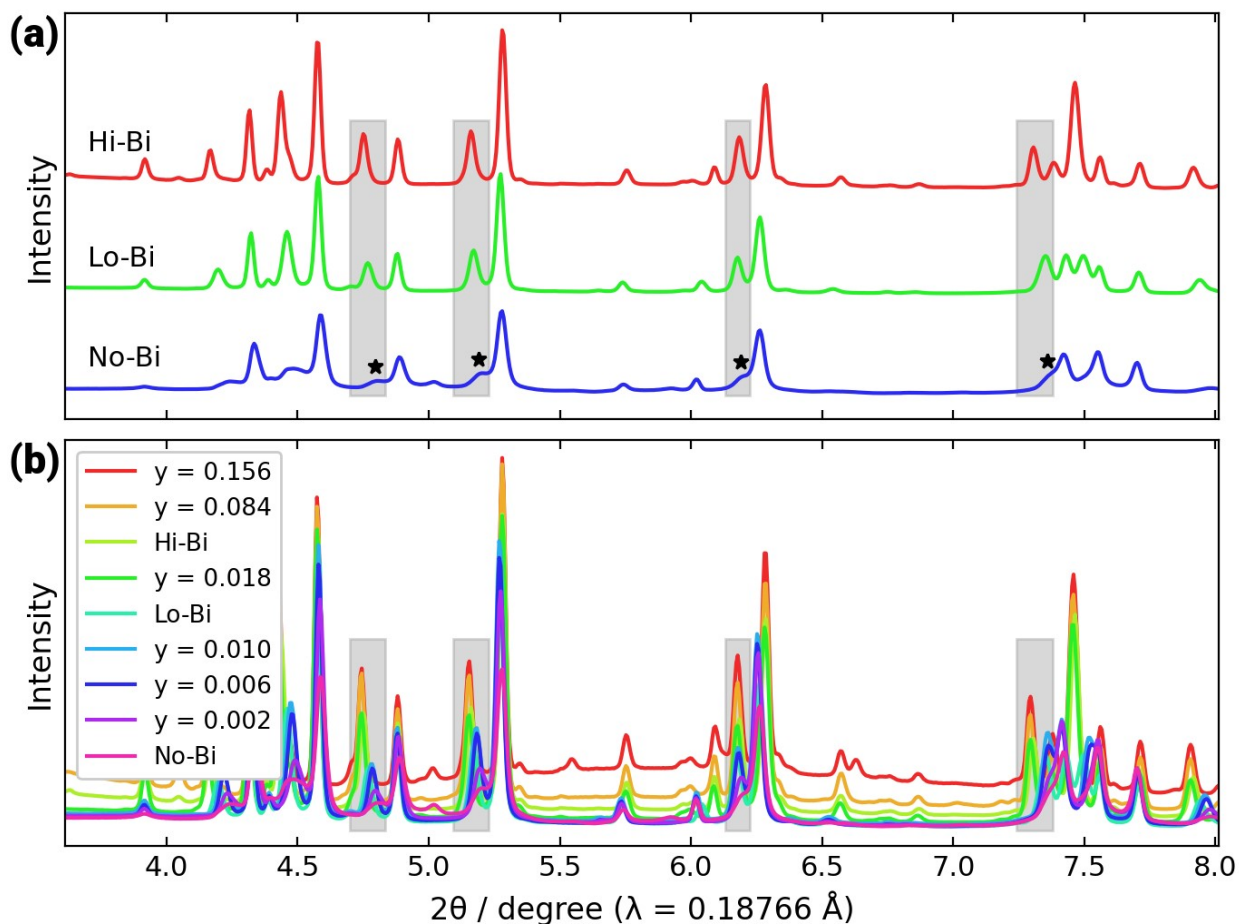| Sample	Formula	a-axis (Å)	b-axis (Å)	c-axis (Å)	Cell volume (Å3)
PDF entry 04-014-5768	$K_{0.314}Mn_{0.983}O_2(H_2O)_{0.5}$	5.155	2.846	14.088	206.70
No-Bi	$K_{0.308}MnO_2(H_2O)_{0.17}$	5.070	2.846	14.30	206.34
Lo-Bi	$K_{0.332}Bi_{0.013}MnO_2(H_2O)_{0.27}$	5.127	2.848	14.243	207.93
Hi-Bi	$K_{0.384}Bi_{0.043}MnO_2(H_2O)_{0.3}$	5.161	2.847	14.131	207.61

Figure S8. XPD of the K_xBi_y-MnO_2 materials plotted in the same range used by Kim *et al.* to computationally model layered MnO_2, for λ = 0.18766 Å. (a) No-Bi, Lo-Bi, and Hi-Bi. Superstructure peaks are highlighted in gray. The progressive increase in intensity and shift to lower values of 2θ is emphasized. (b) The XPD data of all K_xBi_y-MnO_2 samples showing the influence of Bi^{3+} doping. The evolution of these superreflections is highlighted in gray.

Kim *et al.* originally proposed the method for synthesis of highly crystalline K^+ inserted layered MnO_2, the same method used to synthesize No-Bi discussed here.[106] They successfully modeled the XRD pattern computationally, however it was found that there were unaccounted for peaks not represented in the model. Kim *et al.* attributed these unindexed peaks to the presence of superstructures. These peaks were located at 2θ = 40°, 44°, 53°, and 63° in CuKα (corresponding to 2θ = 4.8°, 5.2°, 6.2°, and 7.3° at a wavelength of λ = 0.18766 Å). **Fig S8a** shows these peaks marked by stars in No-Bi and are highlighted in gray for No-Bi, Lo-Bi, and Hi-Bi. **Fig S8b** also highlights these peaks in gray at all concentrations and the shift in 2θ to lower angles and the drastic increase in intensity as Bi^{3+} dopant increases are readily apparent. Kim *et al.* found it necessary to omit measurements at lower 2θ angles to make convergence of the model possible as preferred orientation of the material during XRD measurements lead to a skewed ratio in intensity of the 2θ = 1.5° peak and 2θ = 3.0°. Therefore, the possible presence of superreflections at lower 2θ values were not reported. However, the effects of preferred orientation did affect the relative intensities of other (00ℓ) peaks present at higher values of 2θ. Ultimately, the intensity of the superstructure peaks were low enough to be ignored in the model of Kim *et al.* and still reach successful convergence. However, the significant increase in intensity of these peaks at higher concentrations of Bi^{3+} likely make ignoring them not possible.
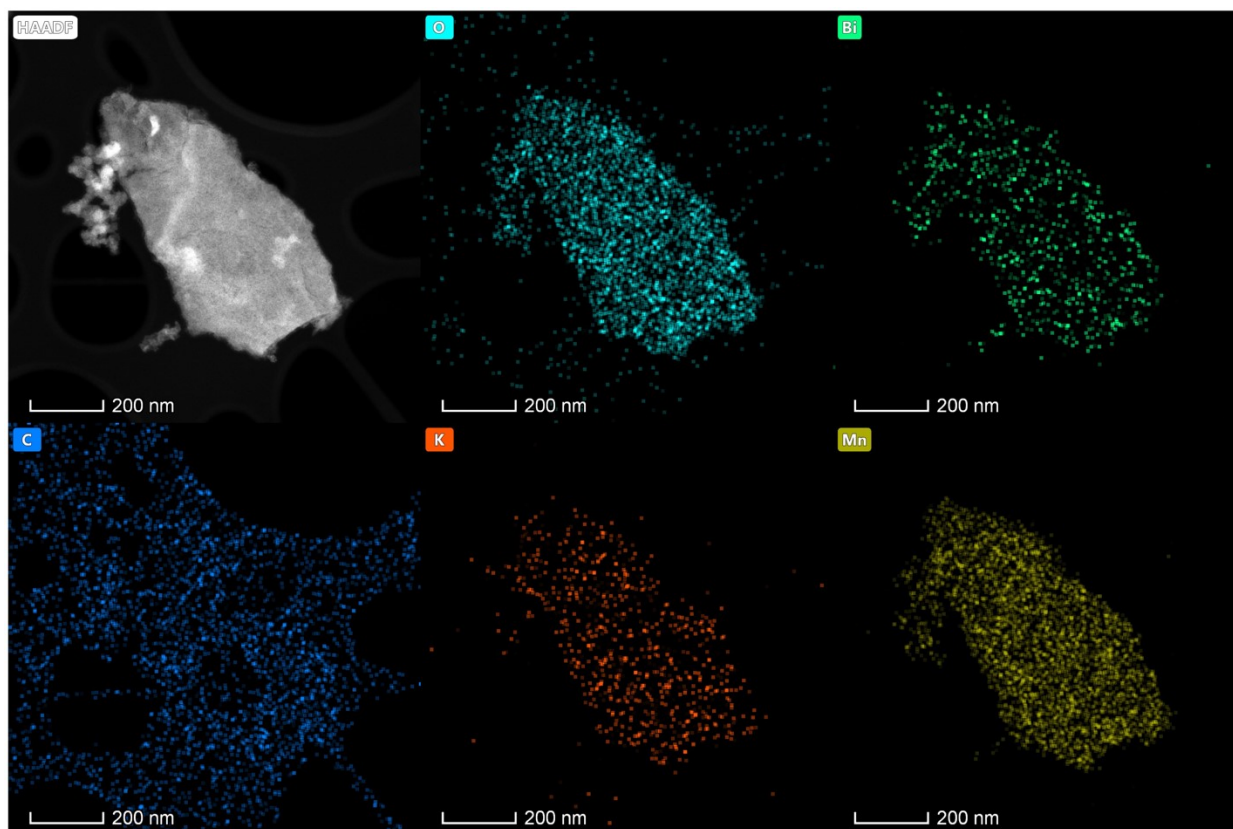
Figure S9. TEM and EDS mapping for elemental species: O, Bi, C, K, and Mn of Ultra Hi-Bi.
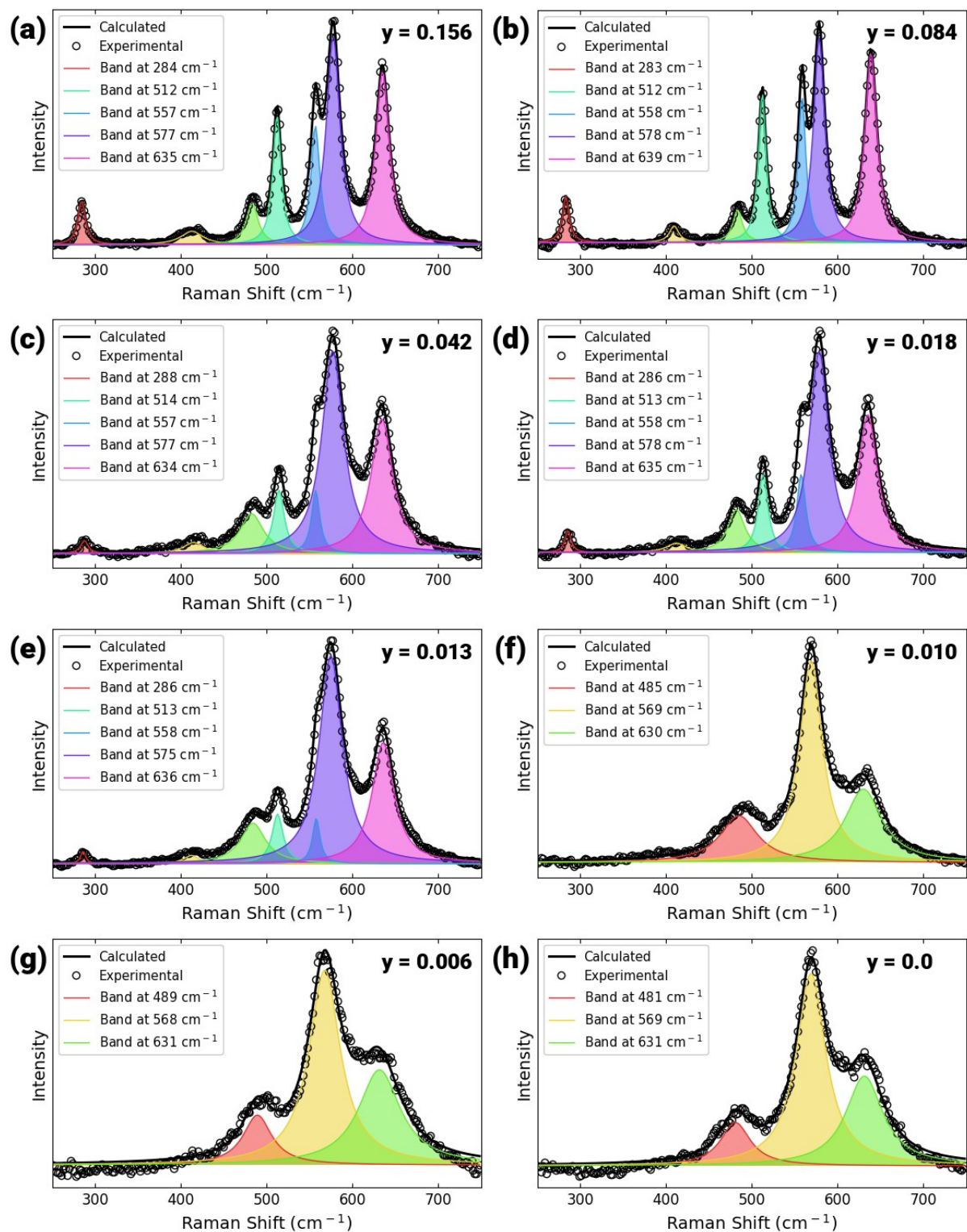
Figure S10. Computationally deconvoluted peaks of K_xBi_y-MnO_2 at (a) y = 0.156, (b) y = 0.084, (c) y = 0.042, (d) y = 0.018, (e) y = 0.013, (f) y = 0.010, (g) y = 0.006, and (h) y = 0.0. Values are given in **Tables S4** and **S5**.

Table S4. Band positions and areal fractions of bands for spectra of K_xBi_y-MnO_2 samples that demonstrated a split of the v_2 (y values equal to or greater than 0.013).

	y = 0.156		y = 0.084		y = 0.042		y = 0.018		y = 0.013	
	band	frac	band	frac	band	frac	band	frac	band	frac
	284 cm^{-1}	0.039	283 cm^{-1}	0.038	288 cm^{-1}	0.010	286 cm^{-1}	0.015	286 cm^{-1}	0.006
v_4	413 cm^{-1}	0.035	409 cm^{-1}	0.020	415 cm^{-1}	0.023	412 cm^{-1}	0.020	412 cm^{-1}	0.013
	483 cm^{-1}	0.058	484 cm^{-1}	0.041	482 cm^{-1}	0.095	482 cm^{-1}	0.081	484 cm^{-1}	0.106
v_3	512 cm^{-1}	0.129	512 cm^{-1}	0.150	514 cm^{-1}	0.071	513 cm^{-1}	0.084	513 cm^{-1}	0.059
	557 cm^{-1}	0.128	558 cm^{-1}	0.152	557 cm^{-1}	0.055	558 cm^{-1}	0.079	558 cm^{-1}	0.037
v_2	577 cm^{-1}	0.334	578 cm^{-1}	0.300	577 cm^{-1}	0.451	578 cm^{-1}	0.431	575 cm^{-1}	0.503
v_1	635 cm^{-1}	0.278	639 cm^{-1}	0.299	634 cm^{-1}	0.294	635 cm^{-1}	0.290	636 cm^{-1}	0.276

Table S5. Band position and areal fraction of each band for K_xBi_y-MnO_2 samples for which it was not possible to find evidence of a second v_2 band using computational deconvolution.

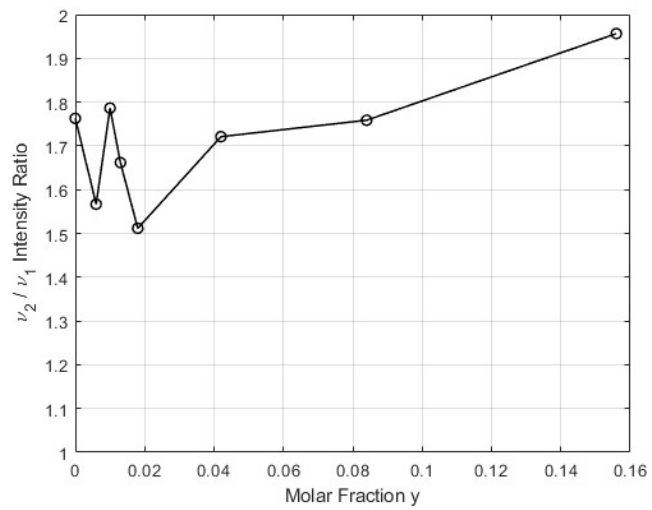|	y = 0.010		y = 0.006		y = 0.0	
	band	frac	band	frac	band	frac
v_3	485 cm^{-1}	0.192	489 cm^{-1}	0.127	481 cm^{-1}	0.128
v_2	569 cm^{-1}	0.518	568 cm^{-1}	0.539	569 cm^{-1}	0.557
v_1	630 cm^{-1}	0.290	631 cm^{-1}	0.334	631 cm^{-1}	0.316

Figure S11. The v_2/v_1 intensity ratio. The intensity increases with increasing molar fraction of y, which is associated with decreasing interlayer spacing.
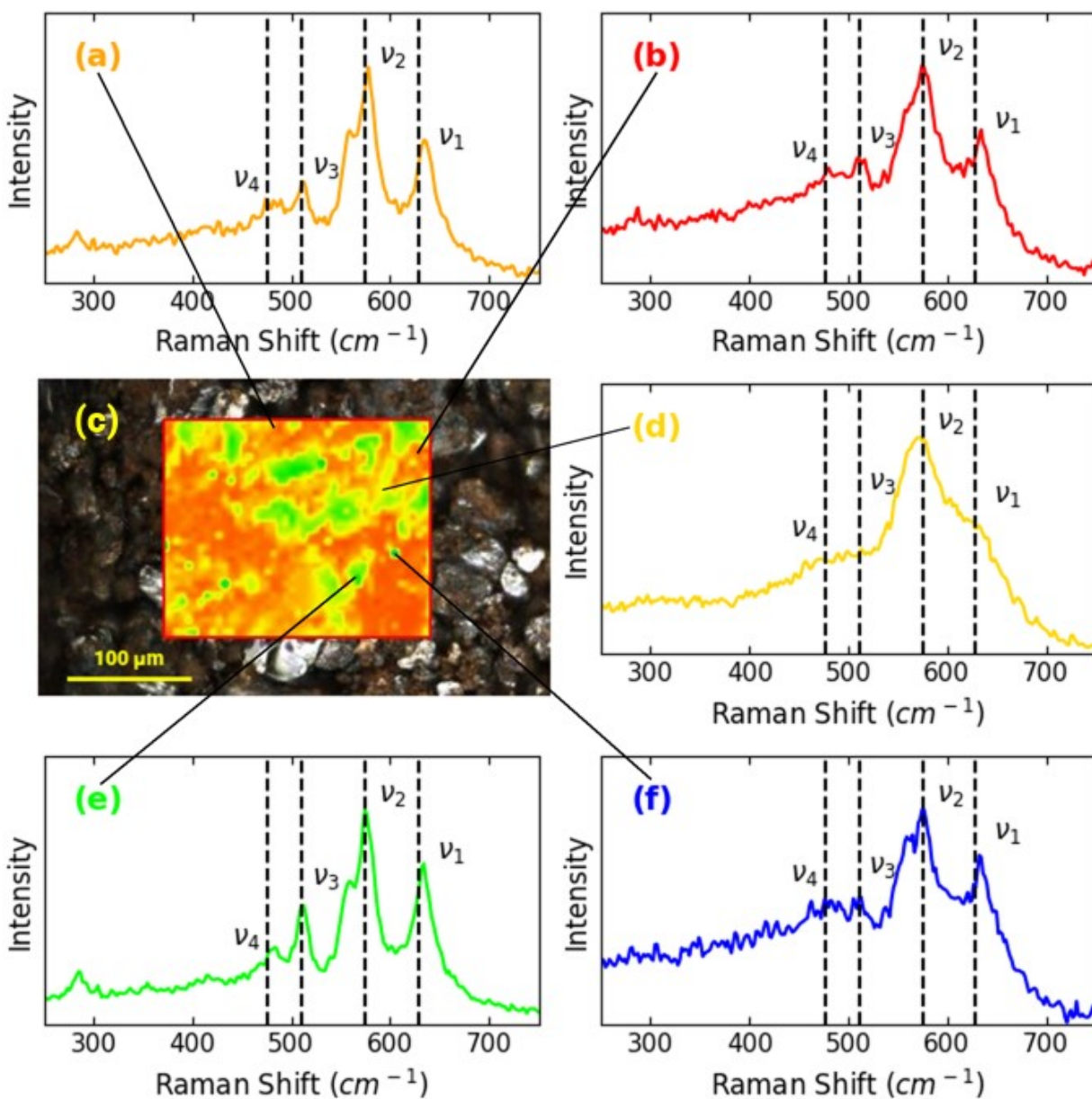
Figure S12. 2D Raman mapping conducted on Hi-Bi. (c) A Raman correlation heat map superimposed on the optical image of the material. The correlation was with a reference spectrum of Hi-Bi. (a, b, d-f) Individual spectra for the indicated regions.

All regions regardless of color gave the expected response for layered manganese oxide. The (a) orange region, (b) red region, (e) green region, and (f) blue region were all very similar, giving evidence of all four bands marked by Julien *et al.* as well as the band at 280 cm⁻¹.[135] The (b) yellow region, gave a Raman response very similar to that of No-Bi as seen in **Fig S10h**. This was likely due to the orientation of Hi-Bi particles. Orientation of the MnO_2 particles relative to the incident light can affect the Raman response measured.[143] This shape-induced effect causes (de)polarization causing band shifting and the change in intensity can be attributed to attenuation of the local internal electromagnetic field.[144] This effect is shown in **Fig S13**.
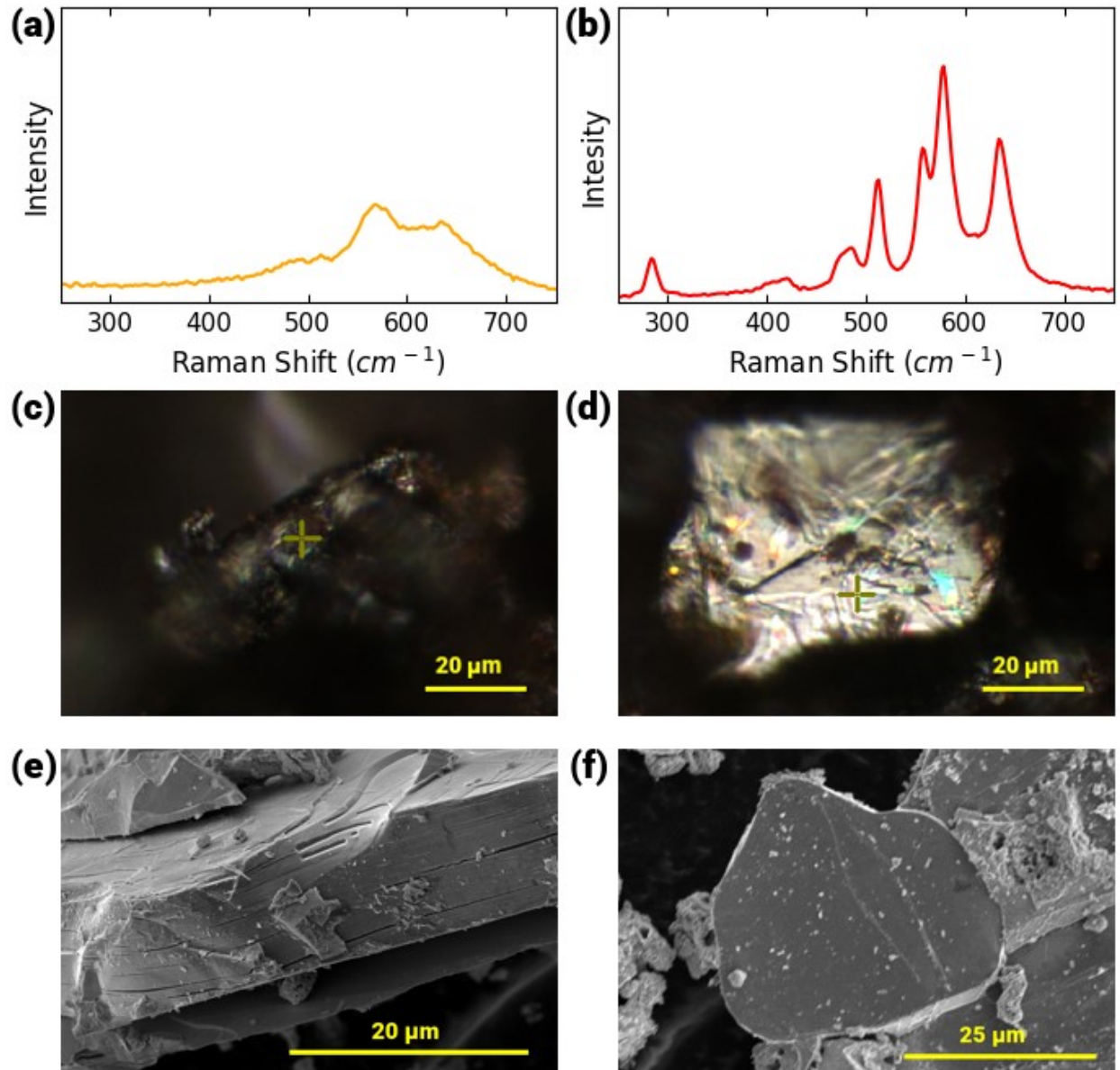
Figure S13. Raman measurements taken on Ultra Hi-Bi showing the effect of particle orientation. The Raman response when the incident light is (a) along to the ab plane and (b) orthogonal to the c plane. Optical images of (c) the ab plane and (d) the c plane are also shown. The yellow cross-hairs in those two images show the location of the incident light for Raman spectra collection. SEM images along the (e) ab plane and orthogonal to the (f) c plane give a better depth of view of Ultra Hi-Bi particles along these directions.

The same material could give quite a different response depending on the orientation of the material. In **Fig S13c** it could be seen that the majority of the particles were oriented with their c planes orthogonal to the optical and incident light source. Given the effects of orientation, Hi-Bi was concluded to have a high degree of homogeneity.
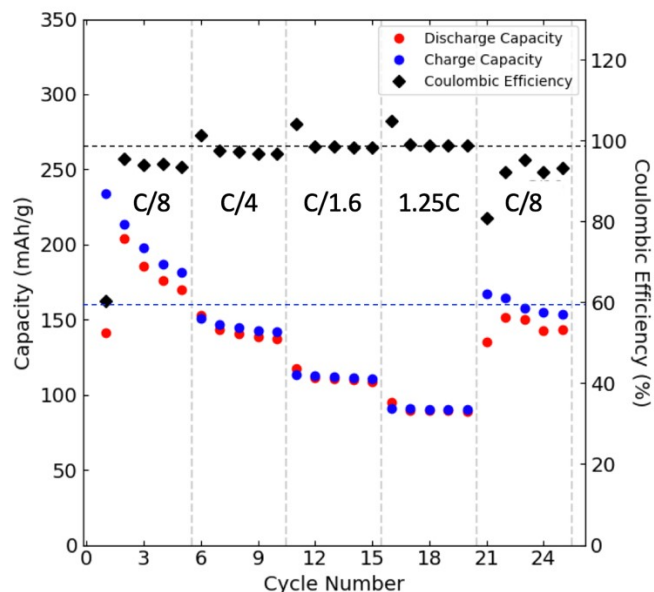
Figure S14. Rate testing of a Lo-Bi cathode in a Li-ion cell. Rates were C/8, C/4, C/1.6 (1h 36m rate), and 1.25C (48m rate) based on 200 mAh/g theoretical capacity.

Fig S14 shows a rate analysis of Lo-Bi material (de)intercalating Li$^+$. The rate study was convoluted with the initial cathode formation period, and in this regime we expected some side reactions causing conversion to LiMn$_2$O$_4$. However, as shown in **Fig 5a**, the specific capacity was expected to settle into a constant value at about cycle 20.

This cell settled into a C/8 capacity of 160 mAh/g. This was somewhat lower performance than the cell in **Fig 5a**, which was at about 190 mAh/g, and this may have been due to the stress of the rate test during electrode formation. The cell was taken through C/8, C/4, C/1.6 (1h 36m rate), and 1.25C (48m rate). These rates assumed a theoretical specific capacity of 200 mAh/g. At the C/1.6 rate the capacity was relatively constant at 110 mAh/g. This meant that moving from an 8h rate to a 1h 36m rate caused a capacity loss of 31%. This was due to additional overpotentials that triggered the voltage limits sooner than at a slower rate.
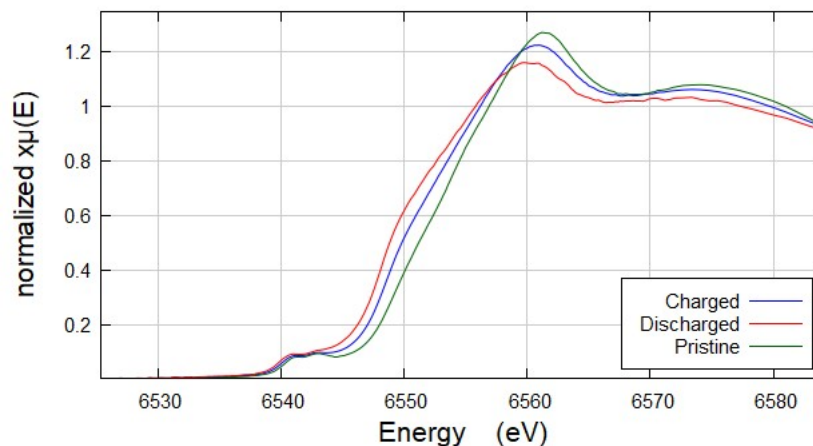
Figure S15. XANES analysis showing the Mn K-edge for cathodes of Li-ion cells prepared with Lo-Bi cathode material. The pristine cathode was as-fabricated. The discharged cathode was subjected to discharge and halted. The charged cathode was discharged and then charged.

To study the mechanism of charge compensation, we analyzed Li-ion batteries prepared with the Lo-Bi material as the cathode host. The cathodes were removed from the cells and tested by XANES analysis at the Mn K-edge at beamline 7-BM (QAS) of the NSLS-II. Three conditions were tested: (a) a pristine cell, which was fabricated but not cycled; (b) a discharged cell; and (c) a charged cell. The XANES results are shown below in **Fig S15**.

The Mn K-edge was observed to shift based on the cycling state. This shift indicated a change in the average Mn oxidation state. This supported a conventional interpretation of the charge compensation reaction, namely that Li^+ was inserted in the interlayer, and to compensate this charge a nearby Mn atom in the MnO_6 slabs was reduced from Mn(IV) to Mn(III). The reverse process occurred during deintercalation. The E0 value is the point where the absorption coefficient began to increase during the XANES energy scan, following the two small pre-edge peaks at 6540 and 6542 eV. The E0 values were 6549.3 eV for pristine; 6548.2 eV for discharged; and 6548.6 eV for charged. This showed the Mn was reduced during discharge and oxidized during charge. The average oxidation state in the charged state did not return to the same value as the pristine material. It was clear from the EDXRD results that some cation exchange occurred between Li^+ and the K^+ initially present in the structure, and that some Mn was converted to a different structure (LMO) although the LMO fraction was relatively small in differential capacity plots.
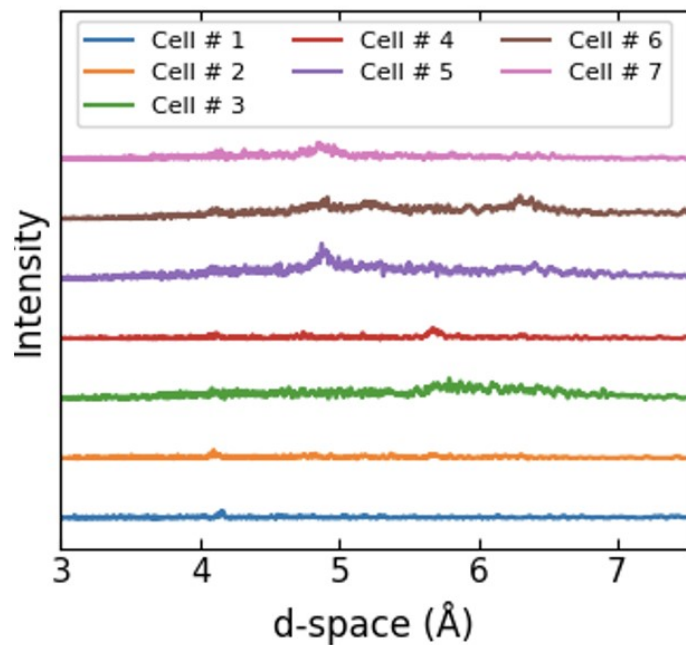
Figure S16. EDXRD data of seven different No-Bi cathodes in the stainless steel casing. Results showed that little to no layered MnO_2 of sufficiently high crystallinity was detected.
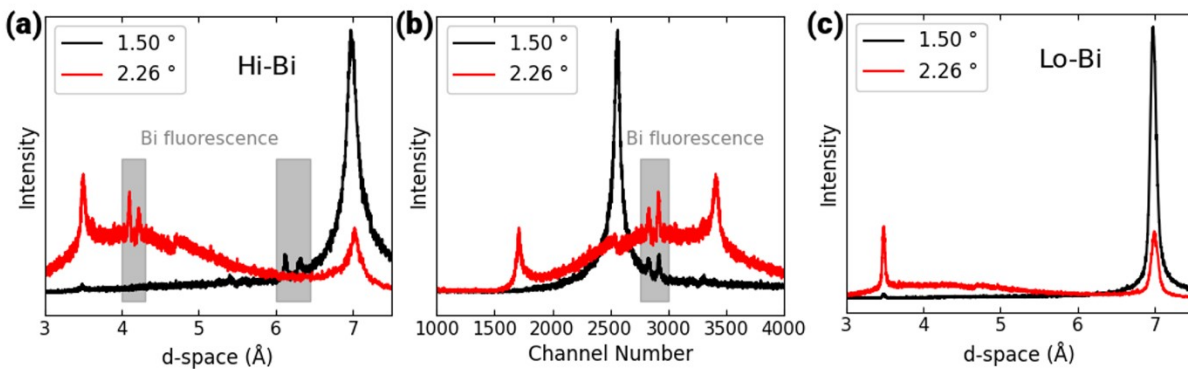
Figure S17. (a-b) EDXRD measurements of a Hi-Bi cathode delaminated from its aluminum foil current collector taken at 1.5° as well as 2.26° as a standard. (a) When converted to d-space the hydrated 7 Å δ-MnO_2 layered structure was confirmed by its characteristic peaks at 7 Å and 3.5 Å. (b) The peaks caused by Bi fluorescence were confirmed when viewing the raw data in channel number where the fluorescence peaks overlap as these artifacts are independent of the measurement angle. (c) The 7 Å and 3.5 Å peaks were also confirmed in a delaminated Lo-Bi cathode. In this case the Bi concentration was not high enough to produce observable fluorescence peaks.
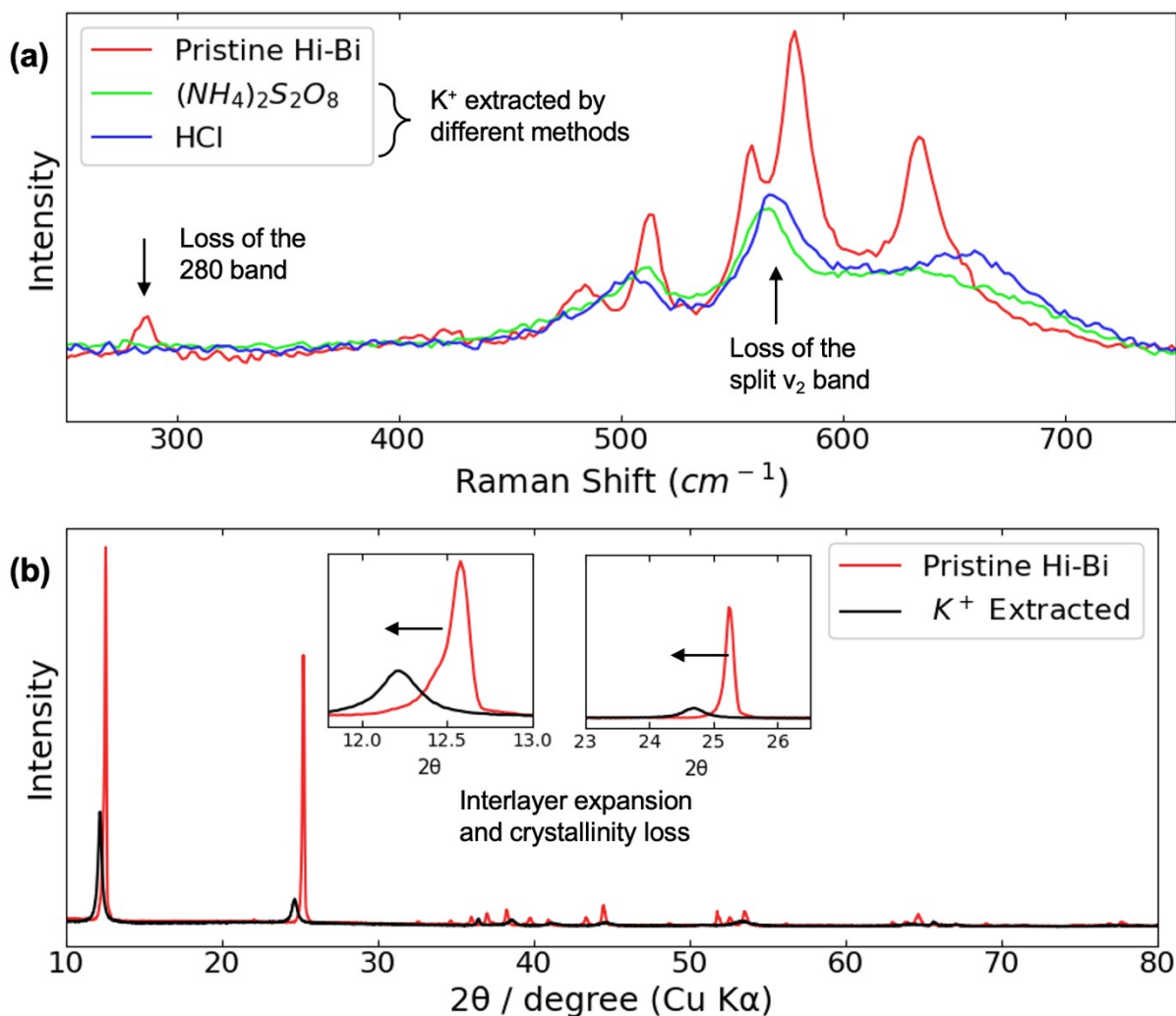
Figure S18. (a) Raman spectra of Bi^{3+} doped δ-MnO_2 before K^+ extraction (red curve), after K^+ extraction using the method proposed by Yang *et al.* (green curve), and after K^+ extraction using the method proposed by Hatakeyama *et al.*[123,124] (b) XRD measurements of Bi^{3+} doped MnO_2 before K^+ extraction (red curve) and after K^+ extraction (black curve). Inset to emphasize the shift of the two characteristic peaks at around 2θ = 12.5 ° and 2θ = 25 ° to lower values of 2θ.

Thermal decomposition of $KMnO_4$ leads to a K^+ inserted layered MnO_2. Extraction of these interlayer K^+ prior to cathode fabrication could increase charge/discharge capacities through making insertion sites accessible which would otherwise be occupied by interlayer K^+. Two methods are reported in the literature. A modified method proposed by Yang *et al.* was used to extract K^+.[123] Both methods of K^+ extraction were attempted on Bi^{3+} doped δ-MnO_2 (Hi-Bi). Raman spectra of pristine material as well as products of both K^+ extraction methods are shown in **Fig S18a**. Given the similarities between the Raman spectra of the K^+ extracted materials the two methods are considered equivalent. The reduced overall intensity in Raman response in the K^+ extracted materials can be attributed to amorphization of the layered structure caused by interlayer cation chemical removal.[124,125] **Fig S18b** shows XRD measurements of pristine Bi^{3+} doped layered MnO_2 before and after K^+ extraction. The peak at 2θ = 12.6 ° shifted to 2θ = 12.2 ° after K^+ extraction indicating a significant expansion of interlayer spacing from 7.0 Å to 7.3 Å.
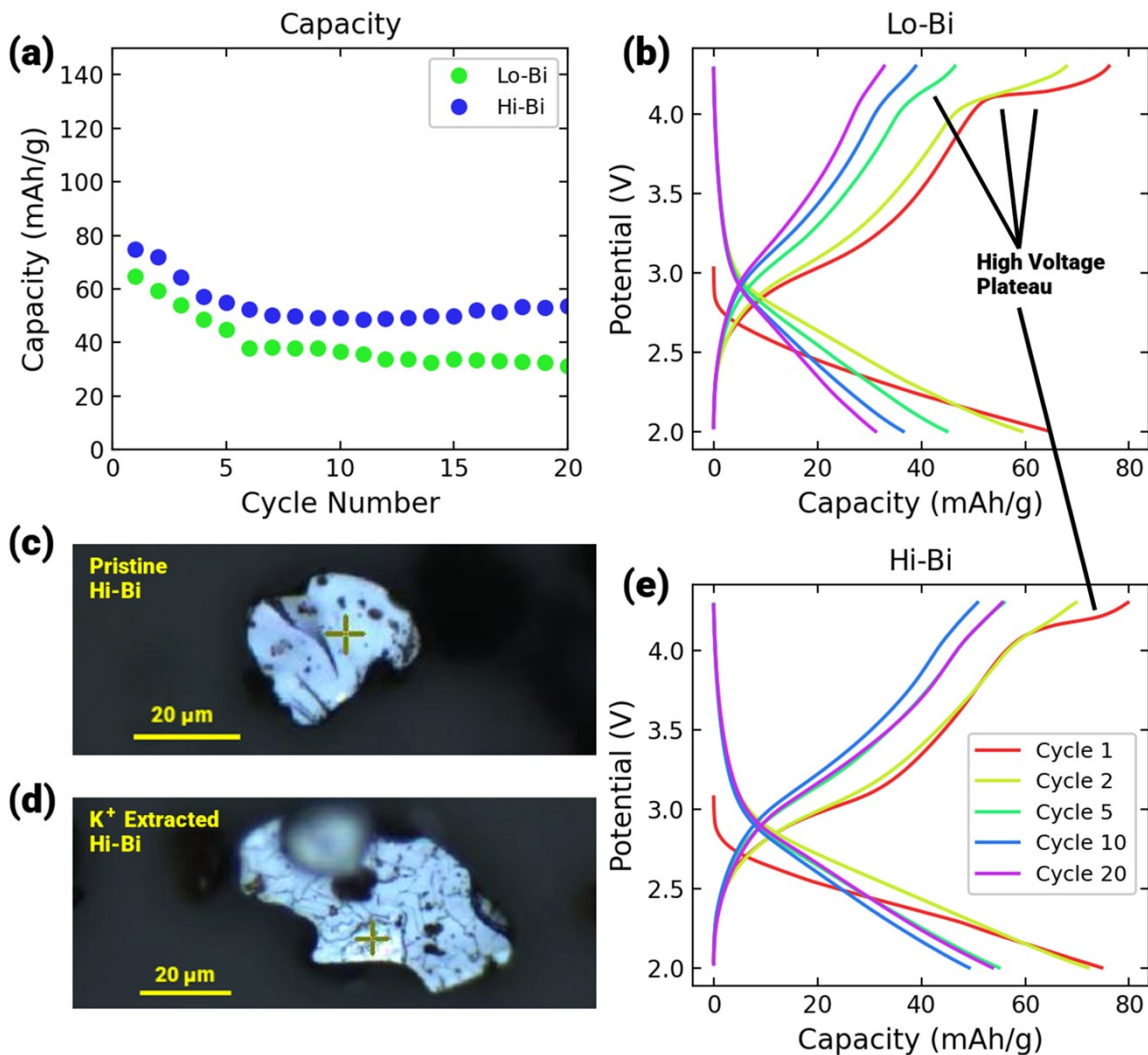
Figure S19. (a) The capacities of K$^+$ extracted Lo-Bi and Hi-Bi Li-ion coin cells discharged at a rate of 23 mA/g are compared. (b) Voltage curves of select cycles of Lo-Bi show the presence of high voltage plateaus. (c) Optical images of pristine Hi-Bi. (d) Optical images of K$^+$ extracted Hi-Bi. Formation of cracks on the surface after K$^+$ extraction is apparent. (e) Voltage curves of select cycles of Hi-Bi. The absence of high voltage plateaus beyond the first cycle was seen in Hi-Bi, similar to the material that was not K$^+$ extracted.

Removal of K$^+$ from the interlayer of K$_x$Bi$_y$-MnO$_2$ would leave the pillaring Bi^{3+} and allow more interlayer sites for Li$^+$ intercalation, so this was attempted. However, it was found that this resulted in reduced performance, as the large K$^+$ played a role in pillaring with the Bi^{3+}.[2, 8, 9] **Fig S18** shows characterization of the K$^+$ extracted material. K$^+$ extraction caused loss of the split v_2 and v_3 bands in the Raman spectrum, and loss of the 280 cm^{-1} band. This demonstrated the split v_3 was due to K$^+$ and the split v_2 and 280 cm^{-1} band were due to the presence of both K$^+$ and Bi^{3+} in the structure. XRD showed that K$^+$ extraction caused an interlayer expansion and loss of crystallinity. This resulted in cracking of the material.[10, 11] Poor electrochemical performance of the K$^+$ extracted cells (<100 mAh/g) is shown in **Fig S19**. However, it was of interest that even in the K$^+$ extracted system, the Hi-Bi had reduced high voltage plateaus on charge. The presence of Bi^{3+} on its own inhibited this conversion, which may have been the electrochemical formation of low periodicity spinel.

4. Supplemental References

1.   Yang, X.; Tang, W.; Feng, Q.; Ooi, K., "Single crystal growth of birnessite-and hollandite-type manganese oxides by a flux method." *Crystal growth & design,* **2003,** *3* (3), 409-415.

2.   Hatakeyama, T.; Okamoto, N. L.; Ichitsubo, T., "Thermal stability of MnO2 polymorphs." *Journal of Solid State Chemistry,* **2022,** *305*, 122683.

3.   Bach, S.; Pereira-Ramos, J.; Baffier, N., "Synthesis and characterization of lamellar MnO2 obtained from thermal decomposition of NaMnO4 for rechargeable lithium cells." *Journal of Solid State Chemistry,* **1995,** *120* (1), 70-73.

4.   Liu, Y.; Wang, H.; Qian, L.; Zhao, X.; Yao, L.; Wang, J.; Xing, X.; Mo, G.; Chen, Z.; Wu, Z., "Bismuth–iron-based precursor: preparation, phase composition, and two methods of thermal treatment." *RSC advances,* **2020,** *10* (35), 20713-20723.

5.   Pang, J.; Han, Q.; Liu, W.; Shen, Z.; Wang, X.; Zhu, J., "Two basic bismuth nitrates:[Bi6O6 (OH) 2](NO3) 4· 2H2O with superior photodegradation activity for rhodamine B and [Bi6O5 (OH) 3](NO3) 5· 3H2O with ultrahigh adsorption capacity for methyl orange." *Applied Surface Science,* **2017,** *422*, 283-294.

6.   Malmros, G., "The crystal structure of a-Bi2O3." *Acta Chem. Scand,* **1970,** *24* (2), 384.

7.   Blower, S.; Greaves, C., "The structure of β-Bi2O3 from powder neutron diffraction data." *Acta Crystallographica Section C: Crystal Structure Communications,* **1988,** *44* (4), 587-589.

8.   Kempaiah, R.; Chan, H.; Srinivasan, S.; Sankaranarayanan, S. K.; Narayanan, B.; Subramanian, A., "Impact of Stabilizing Cations on Lithium Intercalation in Tunneled Manganese Oxide Cathodes." *ACS Applied Energy Materials,* **2021,** *4* (11), 12099-12111.

9.   Ogata, A.; Komaba, S.; Baddour-Hadjean, R.; Pereira-Ramos, J.-P.; Kumagai, N., "Doping effects on structure and electrode performance of K-birnessite-type manganese dioxides for rechargeable lithium battery." *Electrochimica Acta,* **2008,** *53* (7), 3084-3093.

10.   Bach, S.; Pereira-Ramos, J.; Baffier, N., "Rechargeable 3 V Li cells using hydrated lamellar manganese oxide." *Journal of the Electrochemical Society,* **1996,** *143* (11), 3429.

11.   Alcantara, R.; Lavela, P.; Tirado, J.; Zhecheva, E.; Stoyanova, R., "Recent advances in the study of layered lithium transition metal oxides and their application as intercalation electrodes." *Journal of Solid State Electrochemistry,* **1999,** *3* (3), 121-134.